

Venus water loss is dominated by HCO^+ dissociative recombination

<https://doi.org/10.1038/s41586-024-07261-y>

M. S. Chaffin^{1,3}✉, E. M. Cangi^{1,3}, B. S. Gregory¹, R. V. Yelle², J. Deighan¹, R. D. Elliott¹ & H. Gröller²

Received: 3 October 2023

Accepted: 29 February 2024

Published online: 6 May 2024

 Check for updates

Despite its Earth-like size and source material^{1,2}, Venus is extremely dry^{3,4}, indicating near-total water loss to space by means of hydrogen outflow from an ancient, steam-dominated atmosphere^{5,6}. Such hydrodynamic escape likely removed most of an initial Earth-like 3-km global equivalent layer (GEL) of water but cannot deplete the atmosphere to the observed 3-cm GEL because it shuts down below about 10–100 m GEL^{5,7}. To complete Venus water loss, and to produce the observed bulk atmospheric enrichment in deuterium of about 120 times Earth^{8,9}, nonthermal H escape mechanisms still operating today are required^{10,11}. Early studies identified these as resonant charge exchange^{12–14}, hot oxygen impact^{15,16} and ion outflow^{17,18}, establishing a consensus view of H escape^{10,19} that has since received only minimal updates²⁰. Here we show that this consensus omits the most important present-day H loss process, HCO^+ dissociative recombination. This process nearly doubles the Venus H escape rate and, consequently, doubles the amount of present-day volcanic water outgassing and/or impactor infall required to maintain a steady-state atmospheric water abundance. These higher loss rates resolve long-standing difficulties in simultaneously explaining the measured abundance and isotope ratio of Venusian water^{21,22} and would enable faster desiccation in the wake of speculative late ocean scenarios²³. Design limitations prevented past Venus missions from measuring both HCO^+ and the escaping hydrogen produced by its recombination; future spacecraft measurements are imperative.

To assess present-day Venus H loss, we adapted to Venus an existing 1D photochemical model for Mars²⁴ that incorporates both deuterium chemistry²⁵ and a fully coupled ionosphere model²⁶. We compute species densities between 90 and 250 km altitude; key species are shown in Fig. 1 and all species are shown in Extended Data Fig. 1. Most of our model boundary conditions and inputs match previous modelling^{27–29} (see Methods and Extended Data Fig. 2). At the lower boundary, we assume a 1 ppmv water mixing ratio and an $\text{HDO}/\text{H}_2\text{O}$ enrichment 240 times Earth (twice the consensus lower atmosphere D/H) based on Venus Express observations³⁰. Our model is distinguished by our assumption that the upper boundary is closed to all species except H and D, whose upward flux is equal to their self-consistently computed escape rate. Previous dayside models^{28,31,32} used large upper boundary fluxes of H and ion species representing day-to-night transport rather than escape to match the dayside H density inferred from Pioneer Venus Orbiter observations³³. Our intent here is to capture the planet-wide average H and D escape rate resulting from the average abundance of H-bearing and D-bearing species, reflecting the overall balance in the thermosphere/ionosphere system between breaking atomic H and D out of water and diffusing them to lower altitudes at which recombination occurs. Although 3D models exist³⁴, modelling in 1D with a closed upper boundary is sufficient for this purpose because fast thermospheric winds and exospheric transport rapidly mix light species and ions horizontally from the Venus dayside to the nightside on a <10-day timescale³⁵, which is shorter than the vertical eddy mixing timescale at 120 km.

For nonthermal loss, our model predicts that H escape is dominated by HCO^+ dissociative recombination, a process overlooked in previous studies (see Methods and Extended Data Table 1 for a detailed comparison with previous escape work). Figure 2 shows the production rate of escaping hydrogen and deuterium from the five most important loss mechanisms in our model. We compute H and D escape for each mechanism as the product of the rate of the source reaction and the probability that the resulting hot atom escapes before it thermalizes (see Methods). Independent of our model assumptions, HCO^+ dissociative recombination is favoured as an H loss process because of the large proton affinity of CO (ref. 36), which diminishes the abundance of free H⁺. Previous models omitting HCO^+ therefore likely overestimated H escape via resonant charge exchange.

The importance of HCO^+ for H loss and our high predicted HCO^+ density motivate validation of our model against the measured HCO^+ abundance, but such measurements have never been made. On Pioneer Venus, the Orbiter Ion Mass Spectrometer could only measure 16 preselected integer mass/charge ratios insensitive to HCO^+ and unalterable in flight³⁷, whereas the Orbiter Retarding Potential Analyzer (theoretically sensitive to all ions) could in practice resolve only O^+ , O_2^+ , CO_2^+ and the sum of mass/charge 28–30, reported as M29^+ to indicate contributions from N_2^+ , CO^+ and NO^+ (ref. 38). On Venus Express, the ion mass analyser had similarly coarse mass resolution and did not sample the ionospheric peak at which HCO^+ recombines to generate escaping hot H (ref. 39). To our knowledge, no instrument team

¹Laboratory for Atmospheric and Space Physics, University of Colorado Boulder, Boulder, CO, USA. ²Lunar and Planetary Laboratory, University of Arizona, Tucson, AZ, USA. ³These authors contributed equally: M. S. Chaffin, E. M. Cangi. ✉e-mail: michael.chaffin@colorado.edu

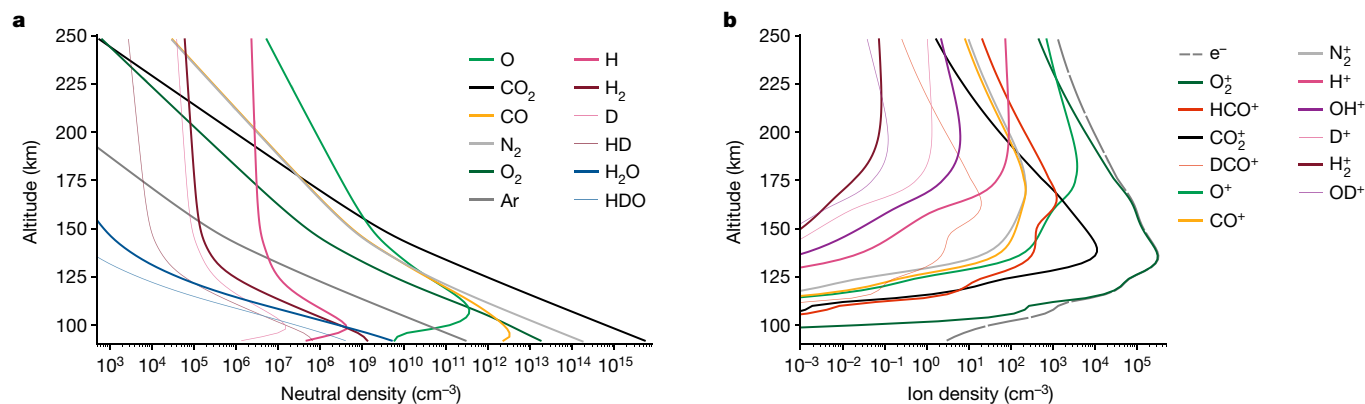


Fig. 1 | Modelled densities for the Venus upper atmosphere. a, Neutral densities, including major H-bearing and D-bearing species. **b**, Ion and electron densities. In both panels, deuterated analogues of H-bearing species are indicated with thin lines.

considered the possibility of substantial HCO⁺ densities, which—in our model—exceed those of similar mass ions. In the absence of HCO⁺ measurements, we validate our predicted H loss rate for HCO⁺ dissociative recombination with an independent photochemical equilibrium argument given in Methods.

For D/H, our fully coupled modelling of H-bearing and D-bearing species results in a thermospheric D/H ratio of 110 times Earth in the atomic species, versus a retrieved value in water of approximately 240 times Earth³⁰ at altitudes of 70–110 km. This depletion of the heavy isotope eases but does not eliminate tensions with the D/H ratio obtained using space telescope observations⁴⁰, which inferred 15–40 times Earth in the thermospheric atomic species from observations indicating a 300 Rayleigh upper limit on the deuterium brightness. Although our isotope ratio is different, our D column is consistent with this brightness upper limit: Pioneer Venus Orbiter data¹⁷ indicate that our planet-average D column should be multiplied by about 0.008 to estimate the dayside column, producing a dayside nadir brightness of roughly 80 Rayleigh for the solar flux reported for the telescope observations⁴⁰. We note that our computed thermospheric D/H ratio is much larger than that produced by one Monte Carlo model¹³, which was consistent with the telescope upper limit⁴⁰, in spite of multiple issues raised about the remote-sensing analysis⁴¹.

Including loss mediated by HCO⁺ nearly doubles previous estimates of the Venus H loss rate (see Extended Data Table 1), requiring a doubled flux of water into the atmosphere from volcanic outgassing and/or water-bearing impactors to maintain a steady state.

Figure 3 shows a schematic water history of Venus, demonstrating that without HCO⁺-driven loss, there is barely enough time since formation for the atmosphere to achieve a steady-state water abundance. With HCO⁺-driven loss, steady state is achieved rapidly. We assume a constant loss rate during blowoff, ending with 100 m of water remaining in the atmosphere. Afterwards, we assume that loss is proportional to the total water column and set the constant of proportionality using the present-day loss rate and inventory (see Methods for a discussion of the rate for each escape process). We further assume that the resupply rate to the atmosphere balances the combined present-day loss rates of the mechanisms considered. Our assumption that contemporary loss is linear in the total water abundance follows past modelling¹⁵ and is also based on initial computational experiments with our model, which demonstrate that increasing the water abundance at the bottom of the thermosphere by a factor of 10 increases the H loss rate via HCO⁺ dissociative recombination by the same factor. It is unclear if this linear dependence would continue at much larger water abundances or when it might saturate (as discussed in ref. 10). When high water concentrations result in a large mixing ratio of H in the thermosphere, an energetic cascade from the approximately 7-eV H atoms produced by HCO⁺ recombination could result in secondary H escape, further boosting loss rates. For ocean scenarios, the higher H loss rates enabled by HCO⁺ dissociative recombination permit the atmosphere to desiccate to its present state more quickly following hydrodynamic escape, improving the prognosis for prolonged oceans (see Extended Data Fig. 3).

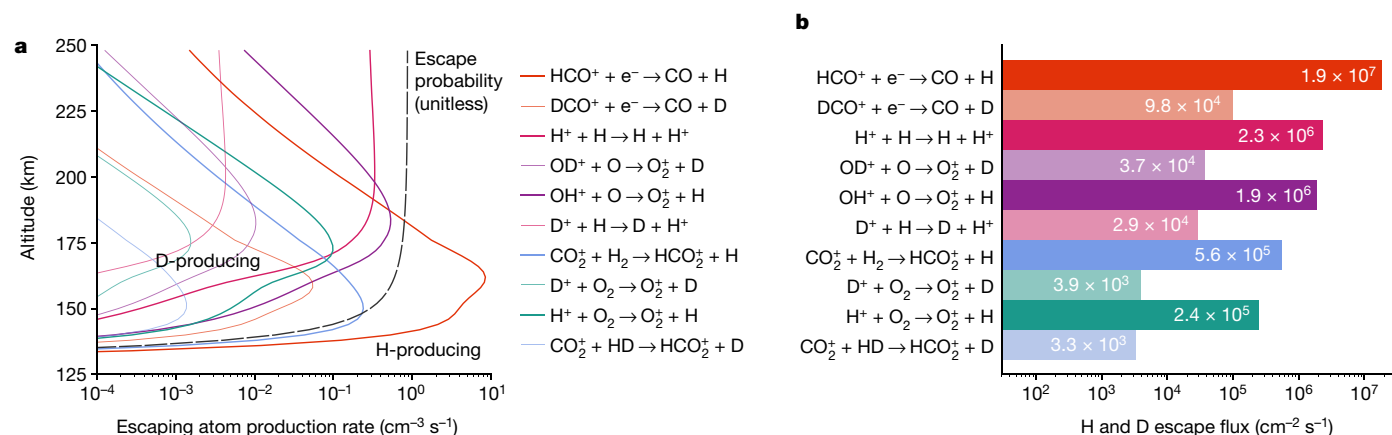


Fig. 2 | Model loss rates for hydrogen and deuterium. a, Altitude profiles of the production rate of escaping atoms. The dashed line shows the likelihood that an energetic H atom produced at a given altitude escapes from the

atmosphere. **b**, Escape flux for each mechanism, computed by vertically integrating the production rate profiles.

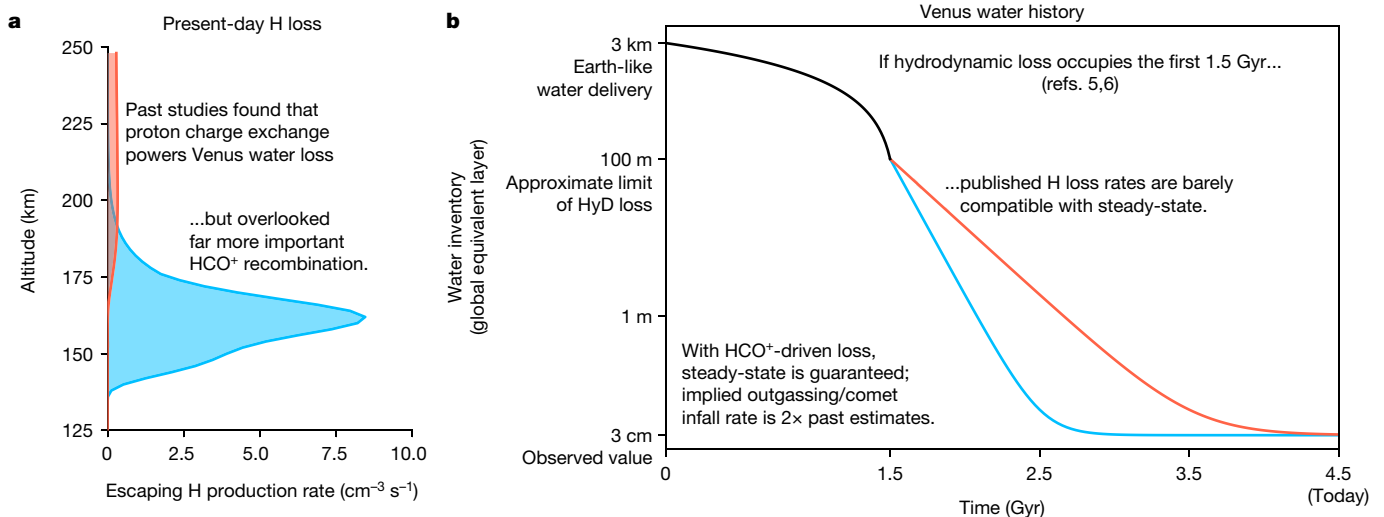


Fig. 3 | Implications of our escape modelling for Venus water history. **a**, Escaping H production rates for the two most important processes in our model. **b**, Schematic water loss history of Venus.

The new photochemical loss channels we investigate enable Venus historical scenarios to match not only the observed bulk water abundance but also the measured $\text{HDO}/\text{H}_2\text{O}$ ratio. Assuming that hydrodynamic escape minimally fractionates D/H (refs. 5,7), all enrichment must occur by means of present-day nonthermal channels. Using a Rayleigh fractionation model^{11,21}, the present isotope enrichment is related to the decline in inventory according to

$$(R/R_0) = (W/W_0)^{f-1}$$

$$f = \frac{\phi_D/\phi_H}{[\text{HDO}]/2[\text{H}_2\text{O}]},$$

in which W represents the past and present water inventory, R the $\text{HDO}/\text{H}_2\text{O}$ ratio in atoms and f the fractionation factor of escape, capturing the relative loss of the isotopes as a fraction of their atomic inventory in water. Our model yields a combined fractionation factor across all escape processes of $f \approx 0.2$, relative to our 90 km lower boundary value of $[\text{HDO}]/2[\text{H}_2\text{O}]$. Adopting $R_0 = \text{Earth D/H}$, there are several possibilities worth discussing. First, desiccation from 100 m of water remaining after hydrodynamic escape to the observed 3 cm at $f = 0.2$ would produce $R \approx 660$ times Earth, much higher than the current consensus. If we take the current enrichment, reservoir and fractionation factor as given, the initial reservoir must have been $W_0 = 10$ m, smaller than the expected remnant from hydrodynamic loss¹⁰. Requiring that desiccation from 100 m to 3 cm produce $R/R_0 = 120$ implies $f \approx 0.4$, which is twice our model value. As mentioned above, our value is computed relative to the observed $\text{HDO}/\text{H}_2\text{O}$ above the cloud tops³⁰, which is roughly double that of the lower atmosphere. In one model⁴², this observed enrichment could be reproduced using artificially prescribed transport and fractionation in photolysis; however, another possibility is that adsorption processes in the clouds, which control the transport of water to the upper atmosphere⁴³, preferentially adsorb the light isotope owing to differences in hydrogen bonding between HDO and H_2O , producing the observed enrichment by means of the same processes that reduce the water mixing fraction by a factor of 30 across the cloud deck. Regardless of the source of the enrichment, computing our model fractionation factor relative to the 120 times Earth value observed in the lower atmosphere gives $f \approx 0.4$, matching the value required by Rayleigh fractionation and providing a consistent (if highly simplified) history satisfying both the inventory and the isotope constraint.

Future measurements and new modelling are urgently needed to understand photochemical H and D loss from the Venus atmosphere to space. Upcoming missions⁴⁴, including DAVINCI, VERITAS and EnVision, will obtain key measurements of the $\text{HDO}/\text{H}_2\text{O}$ ratio in both the well-mixed lower atmosphere and in the neutral atmosphere above the clouds, but will be unable to follow the H and D broken out of this water by photolysis through the upper atmosphere to escape. Because H and D predominantly escape via photochemical processes, in situ measurements extending below the ionospheric peak are required to determine the density of hydrogen-bearing ions that drive H loss, including HCO^+ , as well as the bulk structure of the thermosphere, which prevents some energetic H originating low in the upper atmosphere from escaping. Remote sensing offers the best opportunity to independently measure H and D in the thermosphere and exosphere using the 121.6 nm Lyman α line, either with an echelle grating spectrograph similar to that flown at Mars⁴⁵ or with more compact H and D absorption cells⁴⁶. We note that the H resulting from HCO^+ dissociative recombination will be difficult to detect: the roughly 7 eV excess energy of the reaction produces much faster H than either resonant charge exchange or hot O collisions, resulting in a low-density population that contributes negligibly to the hot H brightness profile, despite its importance for escape⁴⁷. Very-high-resolution spectroscopy sensitive to the H velocity distribution by means of the spectral line shape is the only method likely to unambiguously reveal the low brightness and distinct energy of escaping H resulting from HCO^+ . Past observations of nonthermal hydrogen at Venus^{48–50} have therefore been correctly interpreted as requiring only the lower-energy processes for their explanation. All of the above indicate that, although reanalysis of the Pioneer Venus Orbiter and Venus Express datasets with HCO^+ -driven escape in mind is warranted, for both in situ HCO^+ densities and escaping D/H, the existing dataset is extremely limited. Without new spacecraft measurements, interpretation of the atmospheric water inventory and $\text{HDO}/\text{H}_2\text{O}$ ratio will remain critically dependent on modelling of this poorly sampled mechanism of H and D loss to space.

Online content

Any methods, additional references, Nature Portfolio reporting summaries, source data, extended data, supplementary information, acknowledgements, peer review information; details of author contributions and competing interests; and statements of data and code availability are available at <https://doi.org/10.1038/s41586-024-07261-y>.

1. Izidoro, A. et al. Planetesimal rings as the cause of the Solar System's planetary architecture. *Nat. Astron.* **6**, 357–366 (2022).
2. Salvador, A. et al. Magma ocean, water, and the early atmosphere of Venus. *Space Sci. Rev.* **219**, 51 (2023).
3. Moroz, V. I. et al. Spectrum of the Venus day sky. *Nature* **284**, 243–244 (1980).
4. Marq, E., Mills, F. P., Parkinson, C. D. & Vandaale, A. C. Composition and chemistry of the neutral atmosphere of Venus. *Space Sci. Rev.* **214**, 10 (2018).
5. Kasting, J. F. & Pollack, J. B. Loss of water from Venus. I. Hydrodynamic escape of hydrogen. *Icarus* **53**, 479–508 (1983).
6. Turbet, M. et al. Day–night cloud asymmetry prevents early oceans on Venus but not on Earth. *Nature* **598**, 276–280 (2021).
7. Johnstone, C. P. Hydrodynamic escape of water vapor atmospheres near very active stars. *Astrophys. J.* **890**, 79 (2020).
8. Donahue, T. M., Hoffman, J. H., Hodges, R. R. & Watson, A. J. Venus was wet: a measurement of the ratio of deuterium to hydrogen. *Science* **216**, 630–633 (1982).
9. De Bergh, C. et al. Deuterium on Venus: observations from Earth. *Science* **251**, 547–549 (1991).
10. Kumar, S., Hunten, D. M. & Pollack, J. B. Nonthermal escape of hydrogen and deuterium from Venus and implications for loss of water. *Icarus* **55**, 369–389 (1983).
11. Donahue, T. M. New analysis of hydrogen and deuterium escape from Venus. *Icarus* **141**, 226–235 (1999).
12. Stewart, A. I. F. in *Second Arizona Conference on Planetary Atmospheres* (1968).
13. Hodges, R. R. An exospheric perspective of isotopic fractionation of hydrogen on Venus. *J. Geophys. Res. Planets* **104**, 8463–8471 (1999).
14. Chaufray, J.-Y., Bertaux, J.-L., Quémerais, E., Villard, E. & Leblanc, F. Hydrogen density in the dayside Venusian exosphere derived from Lyman- α observations by SPICAV on Venus Express. *Icarus* **217**, 767–778 (2012).
15. McElroy, M. B., Prather, M. J. & Rodriguez, J. M. Escape of hydrogen from Venus. *Science* **215**, 1614–1615 (1982).
16. Gu, H., Cui, J., Niu, D. & Yu, J. Hydrogen and helium escape on Venus via energy transfer from hot oxygen atoms. *Mon. Not. R. Astron. Soc.* **501**, 2394–2402 (2021).
17. Hartle, R. E. & Grebowsky, J. M. Light ion flow in the nightside ionosphere of Venus. *J. Geophys. Res. Planets* **98**, 7437–7445 (1993).
18. Persson, M. et al. H⁺/O⁺ escape rate ratio in the Venus magnetotail and its dependence on the solar cycle. *Geophys. Res. Lett.* **45**, 10805–10811 (2018).
19. Lammer, H. et al. Loss of hydrogen and oxygen from the upper atmosphere of Venus. *Planet. Space Sci.* **54**, 1445–1456 (2006).
20. Gillmann, C. et al. The long-term evolution of the atmosphere of Venus: processes and feedback mechanisms. *Space Sci. Rev.* **218**, 56 (2022).
21. Grinspoon, D. H. Implications of the high D/H ratio for the sources of water in Venus' atmosphere. *Nature* **363**, 428–431 (1993).
22. Avicé, G. et al. Noble gases and stable isotopes track the origin and early evolution of the Venus atmosphere. *Space Sci. Rev.* **218**, 60 (2022).
23. Way, M. J. & Del Genio, A. D. Venusian habitable climate scenarios: modeling Venus through time and applications to slowly rotating Venus-like exoplanets. *J. Geophys. Res. Planets* **125**, e06276 (2020).
24. Chaffin, M. S., Deighan, J., Schneider, N. M. & Stewart, A. I. F. Elevated atmospheric escape of atomic hydrogen from Mars induced by high-altitude water. *Nat. Geosci.* **10**, 174–178 (2017).
25. Cangi, E. M., Chaffin, M. S. & Deighan, J. Higher Martian atmospheric temperatures at all altitudes increase the D/H fractionation factor and water loss. *J. Geophys. Res. Planets* **125**, e06626 (2020).
26. Cangi, E., Chaffin, M., Yelle, R., Gregory, B. & Deighan, J. Fully coupled photochemistry of the deuterated ionosphere of Mars and its effects on escape of H and D. *J. Geophys. Res. Planets* **128**, e2022JE007713 (2023).
27. Yung, Y. L. & Demore, W. B. Photochemistry of the stratosphere of Venus: implications for atmospheric evolution. *Icarus* **51**, 199–247 (1982).
28. Fox, J. L. & Sung, K. Y. Solar activity variations of the Venus thermosphere/ionosphere. *J. Geophys. Res. Space Phys.* **106**, 21305–21335 (2001).
29. Krasnopolsky, V. A. A photochemical model for the Venus atmosphere at 47–112 km. *Icarus* **218**, 230–246 (2012).
30. Fedorova, A. et al. HDO and H₂O vertical distributions and isotopic ratio in the Venus mesosphere by Solar Occultation at Infrared spectrometer on board Venus Express. *J. Geophys. Res. Planets* **113**, E00B22 (2008).
31. Paxton, L. J., Anderson Jr, D. E. & Stewart, A. I. F. Analysis of Pioneer Venus Orbiter ultraviolet spectrometer Lyman α data from near the subsolar region. *J. Geophys. Res. Space Phys.* **93**, 1766–1772 (1988).
32. Fox, J. L. The post-terminator ionosphere of Venus. *Icarus* **216**, 625–639 (2011).
33. Brinton, H. C. et al. Venus nighttime hydrogen bulge. *Geophys. Res. Lett.* **7**, 865–868 (1980).
34. Martinez, A. et al. Exploring the variability of the Venusian thermosphere with the IPSL Venus GCM. *Icarus* **389**, 115272 (2023).
35. Navarro, T. et al. Venus' upper atmosphere revealed by a GCM: I. Structure and variability of the circulation. *Icarus* **366**, 114400 (2021).
36. Fox, J. L. The chemistry of protonated species in the Martian ionosphere. *Icarus* **252**, 366–392 (2015).
37. Taylor, H. A., Brinton, H. C., Wagner, T. C. G., Blackwell, B. H. & Cordier, G. R. Bennett ion mass spectrometers on the Pioneer Venus Bus and Orbiter. *IEEE Tran. Geosci. Remote Sens.* **18**, 44–49 (1980).
38. Miller, K. L., Knudsen, W. C. & Spenser, K. The dayside Venus ionosphere: I. Pioneer-Venus retarding potential analyzer experimental observations. *Icarus* **57**, 386–409 (1984).
39. Barabash, S. et al. The Analyser of Space Plasmas and Energetic Atoms (ASPERA-4) for the Venus Express mission. *Planet. Space Sci.* **55**, 1772–1792 (2007).
40. Bertaux, J. L. & Clarke, J. T. Deuterium content of the Venus atmosphere. *Nature* **338**, 567–568 (1989).
41. Donahue, T. M. Deuterium on Venus. *Nature* **340**, 513–514 (1989).
42. Liang, M.-C. & Yung, Y. L. Modeling the distribution of H₂O and HDO in the upper atmosphere of Venus. *J. Geophys. Res. Planets* **114**, E00B28 (2009).
43. Parkinson, C. D. et al. Photochemical control of the distribution of Venusian water. *Planet. Space Sci.* **113**, 226–236 (2015).
44. Widemann, T. et al. Venus evolution through time: key science questions, selected mission concepts and future investigations. *Space Sci. Rev.* **219**, 56 (2023).
45. McClintock, W. E. et al. The Imaging Ultraviolet Spectrograph (IUVS) for the MAVEN Mission. *Space Sci. Rev.* **195**, 75–124 (2015).
46. Bertaux, J. L., Goutail, F., Dimarellis, E., Kockarts, G. & van Ransbeeck, E. First optical detection of atomic deuterium in the upper atmosphere from Spacelab 1. *Nature* **309**, 771–773 (1984).
47. Gregory, B. S., Elliott, R. D., Deighan, J., Gröller, H. & Chaffin, M. S. HCO⁺ dissociative recombination: a significant driver of nonthermal hydrogen loss at Mars. *J. Geophys. Res. Planets* **128**, e2022JE007576 (2023).
48. Barth, C. A., Pearce, J. B., Kelly, K. K., Wallace, L. & Fastie, W. G. Ultraviolet emissions observed near Venus from Mariner V. *Science* **158**, 1675–1678 (1967).
49. Anderson, D. E. The Mariner 5 ultraviolet photometer experiment: analysis of hydrogen Lyman alpha data. *J. Geophys. Res.* **81**, 1213–1216 (1976).
50. Takacs, P., Broadfoot, A., Smith, G. & Kumar, S. Mariner 10 observations of hydrogen Lyman alpha emission from the Venus exosphere: evidence of complex structure. *Planet. Space Sci.* **28**, 687–701 (1980).

Publisher's note Springer Nature remains neutral with regard to jurisdictional claims in published maps and institutional affiliations.

Springer Nature or its licensor (e.g. a society or other partner) holds exclusive rights to this article under a publishing agreement with the author(s) or other rightsholder(s); author self-archiving of the accepted manuscript version of this article is solely governed by the terms of such publishing agreement and applicable law.

© The Author(s), under exclusive licence to Springer Nature Limited 2024

Methods

Present H loss mechanisms are required to explain Venus water

If the early solar nebula was as well mixed as dynamical simulations indicate¹, Venus must have received a similar mass mixing ratio and isotopic composition of water as the Earth², requiring that nearly all of its initial approximately 3 km GEL of water be removed to explain the 3 cm of deuterium-enriched water observed today^{10,11,51}. Most of this loss would likely have occurred as fluid H outflow from a hydrogen-dominated upper atmosphere resulting from a moist or runaway greenhouse; such hydrodynamic escape would remove most of the atmospheric water in 1–2 Gyr (ref. 5). At upper atmosphere H concentrations of about 10% or below, efficient cooling by carbon dioxide reduces the upper atmosphere temperature to the point that thermal H escape from Venus is effectively impossible, and hydrodynamic escape is replaced as the dominant H loss channel by a mix of nonthermal processes that are still active today. This transition occurs with approximately 100 m of water still remaining in the atmosphere, which must then be removed quickly enough to explain the present atmospheric state¹⁰. For both stages of H loss, Venus evolution models frequently prescribe diffusion-limited escape^{52–54}, which abstracts the details of loss by assuming that the escaping H flux is proportional to the total mixing ratio of H in all species at the base of the thermosphere. Although this can provide an upper limit, the actual H loss rate may be limited not by the supply of H from below but instead the ability of the thermosphere/ionosphere system to channel the roughly 0.5 eV required for escape into individual H atoms at high altitudes. Although removing the oxygen from an initial Earth-like water inventory remains more difficult^{20,23,54–58}, particularly if the surface is solid during hydrodynamic escape⁵⁹, removing the hydrogen component is by no means trivial. Detailed attention to the actual mechanisms that energize escaping H atoms is therefore needed to understand the transition from a still-wet post-hydrodynamic Venus to the present planet.

Past and present Venus H escape rates and processes

Many studies have examined H escape at Venus^{10,13,15,19,60}, but none have performed a comprehensive survey of all exothermic neutral and ion mechanisms capable of removing H from the atmosphere. In the absence of an authoritative recent review, we summarize here the escape processes explored so far. Most of these were initially investigated as potential sources of the nonthermal H population unambiguously observed in remote-sensing observations of the exosphere at 121.6 nm Lyman α (refs. 48–50). Best studied is resonant charge exchange, in which ionospheric protons collide with thermospheric neutral hydrogen, producing a neutral H population at the ion temperature of $\geq 1,000$ K. The most recent work on this process¹³ was interpreted in ref. 11 as reflecting a column H escape rate of $1.4 \times 10^7 \text{ cm}^{-2} \text{ s}^{-1}$, averaged over both the globe and the solar cycle. Another escape mechanism involves thermal H achieving escape energy by means of collisions with photochemically produced hot oxygen; there is no consensus about the importance of this mechanism. An early study¹⁵ suggested that hot O collisions are the dominant H escape channel, but subsequent studies argued that they should be negligible^{19,61}. Most recently¹⁶, globe-averaged and solar-cycle-averaged H loss rates from hot O collisions of $0.9 \times 10^7 \text{ cm}^{-2} \text{ s}^{-1}$ were found, agreeing within a factor of two with some cases studied in ref. 62. Proton loss, once considered potentially dominant based on the thermospheric calculations in ref. 17, has been shown in refs. 18,20 to be negligible, with rates of $\leq 0.1 \times 10^7 \text{ cm}^{-2} \text{ s}^{-1}$. Some further cherry-picked ion-neutral and recombination reactions that can produce escaping H have been studied in the past, mostly those involving O^+ ions, but these result in minimal loss compared with the mechanisms listed above^{10,19}. As our modelling shows, HCO^+ dissociative recombination results in a dominant contribution to H escape. Extended Data Table 1 summarizes existing estimates for H loss, including this study. Our H loss rate from the HCO^+ channel is

larger than the global and solar-cycle average loss rate of any other process and nearly equal to the sum of the largest estimates from all other processes.

Inferring loss timescales from previous escape estimates

Estimates of contemporary H loss provide one of the few means to constrain the supply rate of water to the Venus atmosphere, with implications for volcanic outgassing, water-bearing impact rates, and the history of the planet's water inventory. At very low H loss rates, the present dry state of the atmosphere is incompatible with Earth-like water delivery because there is not enough time in solar system history to remove the dregs of the oceans left behind after hydrodynamic escape ends. Assuming that the present-day escape rate depends linearly on the atmospheric water abundance, the e -folding timescale for water loss using the maximum rate from all present-day processes studied before our work is $(3 \text{ cm H}_2\text{O GEL}) / (2.5 \times 10^7 \text{ H atoms cm}^{-2} \text{ s}^{-1}) \approx 250 \text{ Myr}$. Linear dependence of loss is unlikely, especially at large H abundances¹⁰, when loss likely becomes limited by either the ionization rate of the atmosphere (for resonant charge exchange) or the large column depth of upper atmosphere hydrogen (which prevents hot O collisions from producing escaping H). Nevertheless, for 100 m of water remaining after hydrodynamic escape ends, previously published hydrogen loss mechanisms require at a minimum 2 Gyr to desiccate the atmosphere to its present state. Including the 1–2 Gyr required for hydrodynamic loss⁵, a minimum of 3–4 Gyr is required for known processes to desiccate Venus to its current state from an initial Earth-like water abundance. Such a long lower limit on the desiccation duration leaves little time for existence of a primordial surface ocean stabilized by cloud-radiative feedbacks^{23,63}. HCO^+ -driven loss roughly halves the e -folding escape timescale of water from the present atmosphere, enabling later ocean scenarios to evolve to the present observed state over solar system history, as described below. If the primordial water of Venus never condensed into oceans⁶ following delivery and outgassing as steam, or if nonthermal loss is sufficiently rapid, the present-day H escape rate likely reflects a steady-state balance between loss to space and supply by means of mantle outgassing and comet impacts²¹. Of these sources, the cometary supply rate is amenable to dynamical estimation²⁰, making the H loss rate useful in estimating the total water flux from the interior to the atmosphere of Venus²¹, alongside other estimates of volcanic activity^{64,65}. Accurate estimation of the magnitude and mechanisms of H loss at Venus is therefore important for understanding not only the atmosphere but also the geology of the planet.

Model inputs

We use a reaction network essentially identical to the H-bearing species network in ref. 36 used for Mars studies but add fully coupled neutrals and singly deuterated analogues for each H-bearing species. We adopt Venus atmospheric parameters appropriate for solar cycle average conditions from ref. 28, averaging their low and high solar activity inputs to obtain electron, ion and neutral temperatures and eddy diffusion rates shown in Extended Data Fig. 2. At the 90 km lower boundary, we adopt density boundary conditions for CO_2 , Ar, CO, O_2 and N_2 from the model in ref. 66 used in ref. 28 as the neutral background atmosphere. We assume the following densities: $[\text{CO}_2]_{90\text{km}} = 9.17 \times 10^{15} \text{ cm}^{-3}$, $[\text{N}_2]_{90\text{km}} = 3 \times 10^{14} \text{ cm}^{-3}$, $[\text{O}_2]_{90\text{km}} = 2.9 \times 10^{13} \text{ cm}^{-3}$, $[\text{Ar}]_{90\text{km}} = 5 \times 10^{11} \text{ cm}^{-3}$ and, finally, $[\text{CO}]_{90\text{km}} = 4.3 \times 10^{10} \text{ cm}^{-3}$. For water, we assume a volume mixing ratio of 1 ppm, yielding $[\text{H}_2\text{O}]_{90\text{km}} = 9.17 \times 10^9 \text{ cm}^{-3}$, and a D/H ratio of 240 times the Earth value, yielding the value $[\text{HDO}]_{90\text{km}} = 6.9 \times 10^8 \text{ cm}^{-3}$ (refs. 30,67). Recall that the D/H ratio is defined with respect to the atomic abundance, with the Earth value in water equal to $^2\text{H}/^1\text{H} = 1/6,420$ (ref. 68). All other species have a downward eddy mixing velocity at the lower boundary, as is common in upper atmosphere models (for example, ref. 29). Our upper boundary is closed to all species except H and D. For thermal H and D loss, we assume Jeans escape using an effusion velocity appropriate to the species mass and upper boundary

temperature, resulting in negligible thermal escape, as well as nonthermal escape (described below). For these boundary conditions, modelling ions and neutrals self-consistently produced an H_2 density at the lower boundary comparable with that assumed in refs. 27,28. Further model details not discussed here can be determined by consulting the archived model code at the location given in the Code Availability statement.

Calculation of nonthermal escape

For all processes, our H escape probability (shown in Fig. 2) is a function only of the overlying atmospheric column density and was determined using a Monte Carlo escape model procedure developed for Mars⁴⁷ and adapted to the size, gravity and bulk atmosphere of Venus. We compute nonthermal loss following the escape probability method in ref. 47, which is similar to that used in ref. 69. For each exothermic reaction that produces H atoms, we compute the production rate of escaping H atoms at each altitude as the product of the local reaction rate computed by the model and the escape probability appropriate to that altitude. Escape probabilities are computed as a function of the local overhead column density N according to $p = 0.868e^{-0.058\sigma N}$, in which $\sigma = 4 \times 10^{-15} \text{ cm}^2$ for H and $4.5 \times 10^{-15} \text{ cm}^2$ for D. The numerical constants in the escape probability result from a fit to a set of discrete outputs from a Monte Carlo calculation of escape probability as a function of altitude, as described in ref. 47. This escape probability curve assumes that all H start with 5 eV at their origin altitude, when—in reality—every reaction producing hot hydrogen would produce a different range of energies depending on the reaction microphysics. We note that, for the two most important mechanisms in our model, this is not likely to strongly affect our results. For HCO^+ dissociative recombination, this assumption actually reproduces the results of a full first-principles Monte Carlo calculation to a high degree of accuracy⁴⁷. For resonant charge exchange, most of the hot H is produced above the collisional atmosphere, so that this assumption has at most a second-order effect for neutrals that originate travelling down into the atmosphere; furthermore, using a lower initial energy more appropriate for this mechanism when computing its escape probability would decrease the likelihood of downward-moving H retaining escape energy after reversing direction in collisions with the background atmosphere, strengthening our conclusion that HCO^+ -driven loss is dominant.

For all mechanisms other than resonant charge exchange, we assume that all of the excess energy of the reaction goes into kinetic energy of the product H. In reality, a very small fraction of the excess energy would go into kinetic energy of the larger product. If the other product is a molecule, a larger fraction of the reaction excess energy could be sequestered in internal degrees of freedom, such as rotation, vibration and electronic excitation. Very little data exist about the branching ratios into such states; when these branching ratios have been investigated, there is often little consensus (see ref. 70 and references therein for an example relevant to HCO^+). Despite the lack of data, it is clear that absent a pathological distribution of branching ratios, the main processes we explore here are likely important mechanisms for escaping hydrogen. As described above, for our dominant mechanism of HCO^+ dissociative recombination, detailed Monte Carlo calculations that incorporate known values for the branching ratio to excited electronic states of CO confirm the predictions of our simplified modelling to within 10%. For the other mechanisms, increased attention to measurements and models of branching ratios would refine our initial estimates.

For resonant charge exchange, we assume that every neutral H produced can escape, even though only a fraction of the protons are moving fast enough to escape before the collision. Assuming that the protons have a Maxwell–Boltzmann distribution (which may not be correct if nonthermal ion heating processes occur above the collisional atmosphere), we can bound the effect of this assumption. At an ion temperature of 700 K, only 0.3% of protons are travelling fast enough to escape speed and at 4,000 K, about 50%. Assuming that

ion temperature is a linear function of solar zenith angle and using the temperatures reported in ref. 71, about 20% of the proton population has sufficient energy to escape. To obtain a more accurate value, weighting the escape fraction as a function of location by the reaction rate of resonant charge exchange would be required, but this would require at least 2D modelling, which is beyond the scope of this work. In conclusion, the overestimate owing to the assumption that all H resulting from resonant charge exchange can escape is a factor of 2–5. Because resonant charge exchange in our model is restricted to occur only below the model upper boundary of 250 km, we underestimate the reaction rate by a factor dependent on the average altitude of the ionopause. In our model, resonant charge exchange has a flat profile between about 190 km and 250 km. Assuming that the same reaction rate applies to higher altitudes up to the average ionopause provides a means to estimate our undercount. According to ref. 72, the ionopause varies between 325 km on the dayside and 1,000 km on the nightside. Assuming a linear variation with solar zenith angle, the area-weighted average altitude is close to 650 km. Therefore, the underestimate owing to the low altitude of the model upper boundary is $(650 - 190)/(250 - 190) = 7.6$. The net effect of overestimating the escape fraction and underestimating the altitude range of the reaction is then likely an underestimate of 1–3 times.

Model output versus state of the art

We have confidence in our model because it is able to reproduce neutral and ion densities observed and modelled in the past. The overall density profiles of the major species reproduce Pioneer Venus measurements of the dayside upper thermosphere^{73–75}, as well as previous models^{27,28}, except for H-bearing species densities, which reflect the global average owing to our assumed boundary conditions, as described above. Our output also reproduces difficulties encountered by previous models in matching the large reported abundance of O/O^+ and the mass-28 ions, as discussed in ref. 28. This should not affect our ability to compute nonthermal H loss rates for comparison with existing calculations based on similar models.

Equilibrium HCO^+ -driven loss estimate

We compute a data-driven estimate of the equilibrium loss rate to independently validate our full photochemical model result. Escaping H production in our model is largest near 160 km, where high production rates of hot H coincide with ease of escape from the atmosphere. At these altitudes, near the ionospheric peak, ion densities are very likely to be in local photochemical equilibrium; also, most of the hot H produced at 160 km escapes from the atmosphere. The high proton affinity of HCO^+ makes it the terminal protonated ion in this region; as such, it is destroyed only by dissociative recombination, which inevitably produces an energetic H atom capable of escape. We can therefore benchmark our model result for HCO^+ -driven loss by computing the local equilibrium production rate of HCO^+ at 160 km, under the well-justified assumption that its production is locally balanced by dissociative recombination loss that produces an escaping H atom. Extended Data Table 2 gives the density of CO_2 , H, CO_2^+ and H^+ , as well as the computed rate of the ion-atom interchange reactions that dominate HCO^+ production in our model. These HCO^+ precursor species densities were measured at 160 km on the dayside and nightside by Pioneer Venus^{33,73–76}, except for the dayside proton density, which we extrapolate from measurements at higher altitudes using the shape of the H^+ profile modelled in ref. 28. Nightside loss is dominant, as is the case for other photochemical H loss mechanisms resulting from the nightside hydrogen bulge, in which cold-trapped H is concentrated to much higher densities than the dayside, more than compensating for the lower energy availability and ionization fraction of the nightside⁷⁷. Remarkably, the day–night average of the model-independent photochemical equilibrium H loss rates in Extended Data Table 2 is within a factor of several of our 1D model loss rate shown in Fig. 2. This adds

weight to our argument in the main text that our modelled H-bearing species densities reflect a global average and provides an independent line of evidence for HCO⁺-driven hydrogen loss. Future 2D or 3D modelling extending that already performed^{34,78} to understand the impact of fast day-to-night transport^{35,79,80} on H-bearing species densities and H escape is needed, as well as new measurements extending those already planned by future spacecraft^{44,81–83}.

Implications for ocean scenarios

Knowledge of the present-day H loss rate can be used to estimate the time since hydrodynamic escape stopped and discriminate between primordial and late water escape scenarios. Faster H escape in either the hydrodynamic or nonthermal phase would reduce the time required to desiccate the planet once escape starts, allowing surface oceans to linger longer. By doubling the H loss rate and halving the *e*-folding timescale of water loss, HCO⁺ dissociative recombination decreases the time required to remove to space the dregs of the oceans left behind following hydrodynamic blowoff. As indicated in Extended Data Fig. 3, this increases the compatibility between long-lived ocean scenarios and the constraint posed by the observed water inventory. After an ocean period with zero assumed loss, these scenarios use the same assumptions as those described in the main text.

Data availability

Tables containing all reactions used in the model, including their adopted rate coefficients and computed column rates, are provided in a supplementary PDF file accessible on the journal website. These rates are also accessible in the archived code repository listed below, which also includes our adopted photo cross-sections and all other source data used in our model. Model densities for all species, computed rates for reactions shown in Fig. 2, assumed temperature and escape probabilities and computed photo rates are provided in Excel format in the online version of the paper; this file also includes data for our illustrative water-inventory timelines. Source data are provided with this paper.

Code availability

All model code is available at github.com/emcangi/VenusPhotochemistry. The version of the model used to prepare the manuscript is archived on Zenodo at <https://doi.org/10.5281/zenodo.10460004>.

51. von Zahn, U., Kumar, S., Niemann, H. & Prinn, R. in *Venus* (eds Hunten D. M., Colin, L., Donahue, T. M. & Moroz, V. I.) 299–430 (Univ. Arizona Press, 1983).
52. Hunten, D. M. The escape of light gases from planetary atmospheres. *J. Atmos. Sci.* **30**, 1481–1494 (1973).
53. Krissansen-Totton, J., Fortney, J. J. & Nimmo, F. Was Venus ever habitable? Constraints from a coupled interior–atmosphere–redox evolution model. *Planet. Sci. J.* **2**, 216 (2021).
54. Warren, A. O. & Kite, E. S. Narrow range of early habitable Venus scenarios permitted by modeling of oxygen loss and radiogenic argon degassing. *Proc. Natl Acad. Sci.* **120**, e2209751120 (2023).
55. Chassefière, E. Hydrodynamic escape of hydrogen from a hot water-rich atmosphere: the case of Venus. *J. Geophys. Res.* **101**, 26039–26056 (1996).
56. Chassefière, E. Loss of water on the young Venus: the effect of a strong primitive solar wind. *Icarus* **126**, 229–232 (1997).
57. Way, M. J. et al. Was Venus the first habitable world of our solar system? *Geophys. Res. Lett.* **43**, 8376–8383 (2016).
58. Gillmann, C. et al. Dry late accretion inferred from Venus's coupled atmosphere and internal evolution. *Nat. Geosci.* **13**, 265–269 (2020).
59. Selsis, F., Leconte, J., Turbet, M., Chaverot, G. & Bolmont, É. A cool runaway greenhouse without surface magma ocean. *Nature* **620**, 287–291 (2023).
60. Fox, J. L. & Bougher, S. W. Structure, luminosity, and dynamics of the Venus thermosphere. *Space Sci. Rev.* **55**, 357–489 (1991).

61. Hodges Jr, R. R. Collision cross sections and diffusion parameters for H and D in atomic oxygen. *J. Geophys. Res.* **98**, 3799–3805 (1993).
62. Shizgal, B. D. Escape of H and D from Mars and Venus by energization with hot oxygen. *J. Geophys. Res.* **104**, 14833–14846 (1999).
63. Yang, J., Boué, G., Fabrycky, D. C. & Abbot, D. S. Strong dependence of the inner edge of the habitable zone on planetary rotation rate. *Astrophys. J.* **787**, L2 (2014).
64. Herrick, R. R. & Hensley, S. Surface changes observed on a Venusian volcano during the Magellan mission. *Science* **379**, 1205–1208 (2023).
65. Rolf, T. et al. Dynamics and evolution of Venus' mantle through time. *Space Sci. Rev.* **218**, 70 (2022).
66. Hedin, A. E., Niemann, H. B., Kasprzak, W. T. & Seiff, A. Global empirical model of the Venus thermosphere. *J. Geophys. Res.* **88**, 73–84 (1983).
67. Bertaux, J.-L. et al. SPICAV on Venus Express: three spectrometers to study the global structure and composition of the Venus atmosphere. *Planet. Space Sci.* **55**, 1673–1700 (2007).
68. Hagemann, R., Nief, G. & Roth, E. Absolute isotopic scale for deuterium analysis of natural waters. Absolute D/H ratio for SMOW. *Tellus* **22**, 712–715 (1970).
69. Lillis, R. et al. Photochemical escape of oxygen from Mars: first results from MAVEN in situ data. *J. Geophys. Res. Space Phys.* **122**, 3815–3836 (2017).
70. Rosati, R. E., Skrzypkowski, M. P., Johnsen, R. & Golde, M. F. Yield of excited CO molecules from dissociative recombination of HCO⁺ and HOC⁺ ions with electrons. *J. Chem. Phys.* **126**, 154302–154302 (2007).
71. Miller, K. L., Knudsen, C. W., Spennner, K., Whitten, R. C. & Novak, V. Solar zenith angle dependence of ionospheric ion and electron temperatures and density on Venus. *J. Geophys. Res. Space Phys.* **85**, 7759–7764 (1980).
72. Brace, L. H. et al. The dynamic behavior of the Venus ionosphere in response to solar wind interactions. *J. Geophys. Res.* **85**, 7663–7678 (1980).
73. Kasprzak, W. T. et al. in *Venus II: Geology, Geophysics, Atmosphere, and Solar Wind Environment* (eds Bougher, S. W. et al.) 225–258 (Univ. Arizona Press, 1997).
74. Niemann, H. B., Kasprzak, W. T., Hedin, A. E., Hunten, D. M. & Spencer, N. W. Mass spectrometric measurements of the neutral gas composition of the thermosphere and exosphere of Venus. *J. Geophys. Res. Space Res.* **85**, 7817–7827 (1980).
75. Fox, J. L. & Kliore, A. J. in *Venus II: Geology, Geophysics, Atmosphere, and Solar Wind Environment* (eds Bougher, S. W. et al.) 161–188 (Univ. Arizona Press, 1997).
76. Grebowsky, J. M., Kasprzak, W. T., Hartle, R. E. & Donahue, T. M. A new look at Venus' thermosphere H distribution. *Adv. Space Res.* **17**, 191–195 (1996).
77. Donahue, T. M., Grinspoon, D. H., Hartle, R. E. & Hodges, R. R. Jr. in *Venus II: Geology, Geophysics, Atmosphere, and Solar Wind Environment* (eds Bougher, S. W. et al.) 385–414 (Univ. Arizona Press, 1997).
78. Stolzenbach, A., Lefèvre, F., Lebonnois, S. & Määttänen, A. Three-dimensional modeling of Venus photochemistry and clouds. *Icarus* **395**, 115447 (2023).
79. Dickinson, R. E. & Ridley, E. C. Venus mesosphere and thermosphere temperature structure: II. Day-night variations. *Icarus* **30**, 163–178 (1977).
80. Seiff, A. Dynamical implications of the observed thermal contrasts in Venus' upper atmosphere. *Icarus* **51**, 574–592 (1982).
81. Garvin, J. B. et al. Revealing the mysteries of Venus: the DAVINCI mission. *Planet. Sci. J.* **3**, 117 (2022).
82. Smrekar, S. E. et al. VERITAS (Venus Emissivity, Radio Science, InSAR, Topography, and Spectroscopy): a selected discovery mission in 53rd Lunar and Planetary Science Conference. LPI contribution no. 2678, id. 1122 (2022).
83. Helbert, J. et al. The VenSpec suite on the ESA Envision mission – a holistic investigation of the coupled surface atmosphere system of Venus in 16th Europlanet Science Congress, id. EPSC2022-374 (2022).

Acknowledgements M.S.C., E.M.C., B.S.G. and R.D.E. were supported by NASA Solar System Workings grant 80NSSC19K0164 and Planetary Science Early Career Award grant 80NSSC20K1081. E.M.C. was also supported by NASA FINESST award 80NSSC22K1326. M.S.C. and E.M.C. thank M. Landis for helpful discussions about water delivery.

Author contributions M.S.C. oversaw the study, performed final model calculations and the photochemical equilibrium calculation and wrote the initial text of the paper. E.M.C. developed the H-bearing and D-bearing photochemical model and nonthermal escape calculation originally used at Mars with a reaction network provided by R.V.Y. and performed initial model calculations for Venus. B.S.G. developed and ran the Monte Carlo model to generate escape probability curves. R.D.E. initially developed the Monte Carlo escape model with support from J.D. and H.G. H.G. performed pilot studies of HCO⁺-driven loss in the Mars atmosphere. All authors contributed to the interpretation and presentation of model results.

Competing interests The authors declare no competing interests.

Additional information

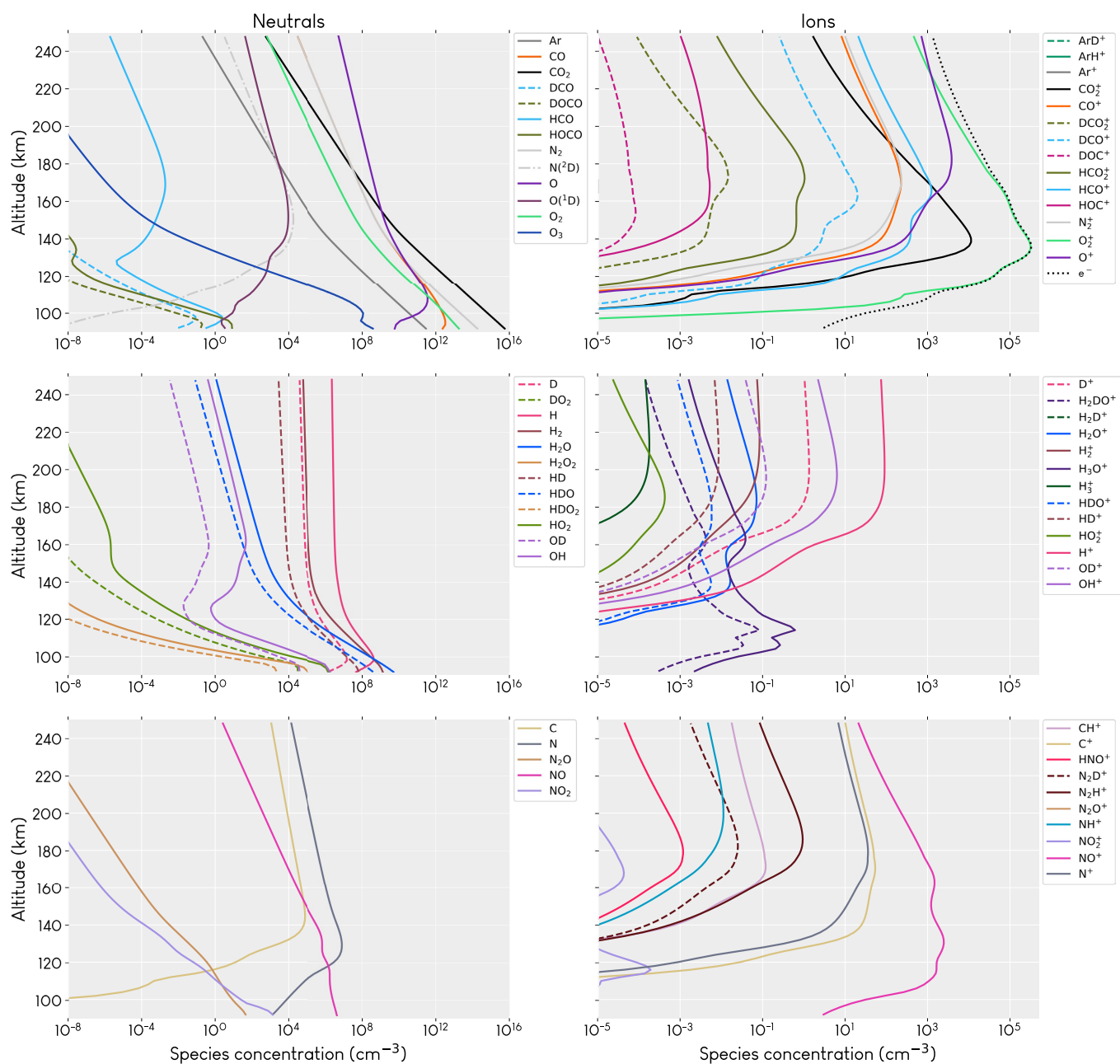
Supplementary information The online version contains supplementary material available at <https://doi.org/10.1038/s41586-024-07261-y>.

Correspondence and requests for materials should be addressed to M. S. Chaffin.

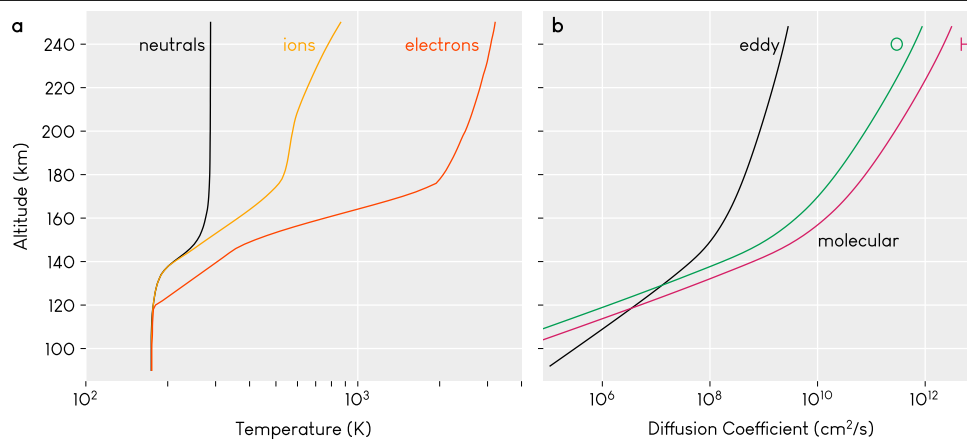
Peer review information Nature thanks David Grinspoon and the other, anonymous, reviewer(s) for their contribution to the peer review of this work. Peer reviewer reports are available.

Reprints and permissions information is available at <http://www.nature.com/reprints>.

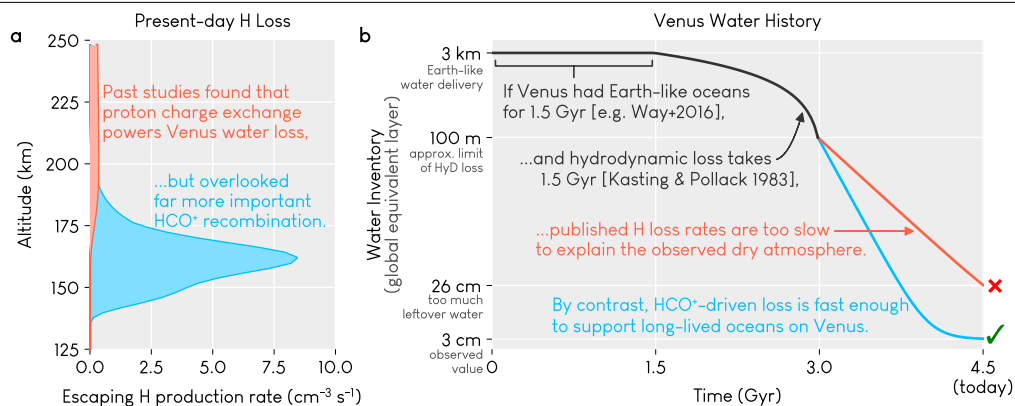
All Model Densities



Extended Data Fig. 1 | Model densities for all species. The six panels function only to separate species for clarity.



Extended Data Fig. 2 | Key photochemical model inputs. a, Temperature profiles for neutrals, ions and electrons adapted from the inputs in ref. 28. **b,** Adopted eddy diffusion profile and molecular diffusion coefficients for H and O atoms.



Extended Data Fig. 3 | Implications of HCO^+ -driven loss for Venus ocean scenarios. **a**, Escaping H production rates for the two most important processes in our model. **b**, Schematic water loss history of Venus.

Extended Data Table 1 | Estimated rates for present-day Venus H loss processes

Process	Rate*	Reference
$\text{HCO}^+ + \text{e}^-$	1.9	this work
$\text{H}^+ + \text{H}$	0.2 – 0.7	this work
	0.8	Donahue et al. [77]
	1.4	Hodges [13] [†]
	0.5 – 1.0	Lammer et al. [19]
Hot O collisions	0.8	McElroy et al. [15]
	nil	Hodges [61]
	0.5	Shizgal [62]
	nil	Lammer et al. [19]
	0.9	Gu et al. [16]
all other photochemistry	0.3	this work
only $\text{O}^+/\text{CO}_2^+ + \text{H}_2$, $\text{OH}^+/\text{CO}_2\text{H}^+ + \text{e}^-$	$\lesssim 0.1$	Lammer et al. [19]
H^+ Ion Loss	0.1	Persson et al. [18]

* Global and solar-cycle average H loss rate in $10^7 \text{ cm}^{-2} \text{ s}^{-1}$

[†] Hodges [13] as averaged by Donahue [11], neutral loss only.

Extended Data Table 2 | Data-driven validation of full model output

Precursor Species	Density at 160 km (cm ⁻³)		Reference
	Day	Night	
CO ₂	3 × 10 ⁹	1 × 10 ⁸	Kasprzak et al. [69], Niemann et al. [70]
H	5 × 10 ⁵	5 × 10 ⁷	Kasprzak et al. [69], Brinton et al. [33], Grebowsky et al. [72]
CO ₂ ⁺	1 × 10 ⁴	1 × 10 ²	Fox & Kliore [71]
H ⁺	5 × 10 ⁻²	1 × 10 ²	Fox & Kliore [71], Fox & Sung [28]
Reaction	Rate (cm ⁻³ s ⁻¹)		Notes
	Day	Night	
CO ₂ ⁺ + H $\xrightarrow{k_1}$ HCO ⁺ + O	2.3	2.3	k ₁ = 4.5 × 10 ⁻¹⁰ cm ³ s ⁻¹ , from Fox [36]
H ⁺ + CO ₂ $\xrightarrow{k_2}$ HCO ⁺ + O	0.6	38	k ₂ = 3.8 × 10 ⁻⁹ cm ³ s ⁻¹ , from Fox [36]
Total HCO ⁺ production ≈ HCO ⁺ loss via HCO ⁺ + e ⁻ ≈ Escaping H production	2.9	40	compare to ~8 cm ⁻³ s ⁻¹ at 160 km in Figure 2

Entries give the measured or inferred densities of HCO⁺ precursor species in the Venus atmosphere and the implied model-independent escaping H production rate at 160 km.